



CHALMERS
UNIVERSITY OF TECHNOLOGY

In Situ Study the Dynamics of Blade-Coated All-Polymer Bulk Heterojunction Formation and Impact on Photovoltaic Performance of

Downloaded from: <https://research.chalmers.se>, 2025-05-17 09:38 UTC

Citation for the original published paper (version of record):

Yao, N., Fan, Q., Wolkeba, Z. et al (2023). In Situ Study the Dynamics of Blade-Coated All-Polymer Bulk Heterojunction Formation and Impact on Photovoltaic Performance of Solar Cells. *Solar RRL*, 7(6).
<http://dx.doi.org/10.1002/solr.202201134>

N.B. When citing this work, cite the original published paper.

In Situ Study the Dynamics of Blade-Coated All-Polymer Bulk Heterojunction Formation and Impact on Photovoltaic Performance of Solar Cells

Nannan Yao,* Qunping Fan, Zewdneh Genene, Heng Liu, Yuxin Xia, Guanzhao Wen, Yusheng Yuan, Ellen Moons, Jan van Stam, Wei Zhang,* Xinhui Lu,* Ergang Wang,* and Fengling Zhang*

All-polymer solar cells (all-PSCs) have achieved impressive progress by employing acceptors polymerized from well performing small-molecule non-fullerene acceptors. Herein, the device performance and morphology evolution in blade-coated all-PSCs based on PBDBT:PF5–Y5 blends prepared from two different solvents, chlorobenzene (CB), and *ortho*-xylene (*o*-XY) are studied. The absorption spectra in CB solution indicate more ordered conformation for PF5–Y5. The drying process of PBDBT:PF5–Y5 blends is monitored by in situ multifunctional spectroscopy and the final film morphology is characterized with ex situ techniques. Finer-mixed donor/acceptor nanostructures are obtained in CB-cast film than that in *o*-XY-cast ones, corresponding to more efficient charge generation in the solar cells. More importantly, the conformation of polymers in solution determines the overall film morphology and the device performance. The relatively more ordered structure in CB-cast films is beneficial for charge transport and reduced non-radiative energy loss. Therefore, to achieve high-performance all-PSCs with small energy loss, it is crucial to gain favorable aggregation in the initial stage in solution.


The limiting factors for all-PSCs are mainly incurred by the small electron mobility of polymer acceptors and strong phase separation upon evaporation of the solvent.^[2,6] It is known that the emerging non-fullerene acceptors (NFAs), such as ITIC and Y6, have strong absorption in the near-infrared region and excellent electron-transport properties, which enables power conversion efficiencies (PCEs) of organic solar cells (OSCs) exceeding 19%.^[7–10] Recently, novel polymer acceptors have been synthesized by polymerizing NFAs to synergize the merits of NFAs and conjugated polymers.^[11–13] The PCEs of all-PSCs employing such polymerized NFAs were promoted to above 16%.^[14,15] However, high-efficient all-PSCs are commonly fabricated via spin-coating in inert atmosphere, which is not compatible with upscaling of solar module production. To realize the commercialization of OSCs in the future, continuous large-area-coating techniques like blade-coating or slot-die-coating are required. Nowadays, the performance of OSCs printed in air still lags behind those of OSCs spin-coated in a glove box.

1. Introduction

All-polymer solar cells (all-PSCs) have attracted extensive attention due to the thermal and mechanical stability of polymers.^[1–5]

N. Yao, Y. Xia, Y. Yuan, F. Zhang
Electronic and Photonic Materials (EFM)
Department of Physics, Chemistry and Biology (IFM)
Linköping University
SE-58183 Linköping, Sweden
E-mail: nannan.yao@liu.se; fengling.zhang@liu.se

Q. Fan, Z. Genene, E. Wang
Department of Chemistry and Chemical Engineering
Chalmers University of Technology
SE-41296 Göteborg, Sweden
E-mail: ergang@chalmers.se

 The ORCID identification number(s) for the author(s) of this article can be found under <https://doi.org/10.1002/solr.202201134>.

© 2023 The Authors. Solar RRL published by Wiley-VCH GmbH. This is an open access article under the terms of the Creative Commons Attribution-NonCommercial License, which permits use, distribution and reproduction in any medium, provided the original work is properly cited and is not used for commercial purposes.

DOI: 10.1002/solr.202201134

H. Liu, X. Lu
Department of Physics
The Chinese University of Hong Kong
Hong Kong 999077, China
E-mail: xinhui.lu@cuhk.edu.hk

G. Wen, W. Zhang
School of Physics and Materials Science
Guangzhou University
Guangzhou 510006, China
E-mail: wzhang@gzhu.edu.cn

E. Moons
Department of Engineering and Physics
Karlstad University
SE-65188 Karlstad, Sweden

J. van Stam
Department of Engineering and Chemical Sciences
Karlstad University
SE-65188 Karlstad, Sweden

As the nanoscale morphology of printed donor–acceptor bulk-heterojunctions (BHJs) is crucial for photovoltaic performance, to enhance device performance, it is necessary to study the dynamics of printed BHJs and figure out key processing parameters for the optimized morphology/phase separation.

The morphology of BHJ active layers is a consequence of the solution-to-solid transition process. The processing conditions such as solvents, additives, and thermal annealing are known to significantly influence the film formation and modulate the final morphology.^[16–18] Studying dynamics of the film formation with an in situ optical spectroscopy can deepen the understanding on BHJs morphology. In situ photoluminescence (PL) spectroscopy could provide information on polymer aggregation/phase evolution from liquids to films by recording the PL spectra evolution of pristine materials. This technique also allows the detection of the donor/acceptor interaction in blends, as the luminescence of the donor (acceptor) could be quenched by charge transfer occurring at the interfaces with the acceptor (donor). A substantial PL quenching typically implies fine-mixed morphology and efficient charge transfer.^[19,20] In situ PL spectroscopy is an unique/effective tool to monitor the morphology formation during the film-drying process, and has been used to study the influence of processing additives, deposition temperature, and annealing treatment on the drying process of BHJs.^[21,22]

It is well known that in morphology evolution such as donor/acceptor miscibility, domain purity significantly affects the charge generation and transport, that can reflect the photocurrent of solar cells. In addition, the degree of order configuration is also important for device fill factor (FF) and open-circuit voltage (V_{OC}). Regarding all-polymer systems, the polymer chain torsion or weak crystallinity brings disorder into the system, resulting in discrete energetic sites and broad density of states (DOS) distribution, that limits charge-hopping transport between adjacent sites.^[18,23–27] Such disorder structure would induce unfavorable non-radiative recombination, which has been demonstrated as the dominating energy loss in OSCs.^[28] Therefore, understanding the morphology formation could also be helpful for further improving the device performance.

In this work, we investigate the correlation between morphology evolution, charge-carrier dynamics, and photovoltaic performance in a blade-coated all-polymer system, poly[(2,6-(4,8-bis(5-(2-ethylhexyl)thiophen-2-yl)-benzo[1,2-b:4,5-b']dithiophene))-alt-(5,5-(1',3'-di-2-thienyl-5',7'-bis(2-ethylhexyl)benzo[1',2'-c:4',5'-c']dithiophene-4,8-dione)] (PBDBT):PF5–Y5. Herein, the PBDBT:PF5–Y5 blend films were processed from chlorobenzene (CB)

and *ortho*-xylene (*o*-XY), the polymer conformation in solutions was studied by absorption spectra. And then in situ PL spectroscopy was used to track the solution-to-solid transition process. Transient absorption (TA) spectroscopy was conducted to explore the charge-transfer process. The morphology of dried films was characterized by atomic-force microscopy (AFM) and grazing-incidence wide-angle X-ray scattering (GIWAXS). Moreover, their influence on device performance was also discussed, especially for the energy loss.

2. Results and Discussion

2.1. Steady-State Absorption Spectroscopy

The absorption spectra of the neat PBDBT, PF5–Y5 (Figure S1, Supporting Information) and PBDBT:PF5–Y5 (4:3 wt%) blend solutions in CB and *o*-XY, as well as the corresponding solid films, are presented in **Figure 1**. The absorption spectra of PBDBT in the two solvents largely overlap with each other with absorption maximum at 620 nm and a shoulder at 578 nm. The absorption spectrum of PF5–Y5 in CB shows an absorption maximum at 740 nm, slightly redshifted spectrum compared to that in *o*-XY at 725 nm, while the onset of absorption is the same in both solvents. We interpret this redshift as an indication for CB being a better solvent for PF5–Y5 than *o*-XY. In a good solvent, the polymer chains tend to extend. A reasonable explanation is that PF5–Y5 in CB has open and extended polymer chain conformation and strong interactions with solvent, that might be favorable to form order structure.^[29] When *o*-XY is used as solvent, in contrast, the polymer is expected to take a more coiled conformation indicating a lower miscibility with *o*-XY. From solution to a solid film the absorption peak of PF5–Y5 displays a pronounced spectral redshift (40 nm for CB or 55 nm for *o*-XY) and the absorption spectrum for the film is independent of the casting solvent. For the absorption maximum of PBDBT, there is only a very small shift (5 nm) to lower energies upon transition from solution to film and the shoulder peak gets more pronounced. These differences are also present in the blends, indicating that the presence of both polymers in the blend does not influence the energy levels of the polymers, as compared to when they are not blended.

2.2. In Situ PL Spectroscopy

Would these different conformations in the two solutions be maintained into their solid films? This transition process was

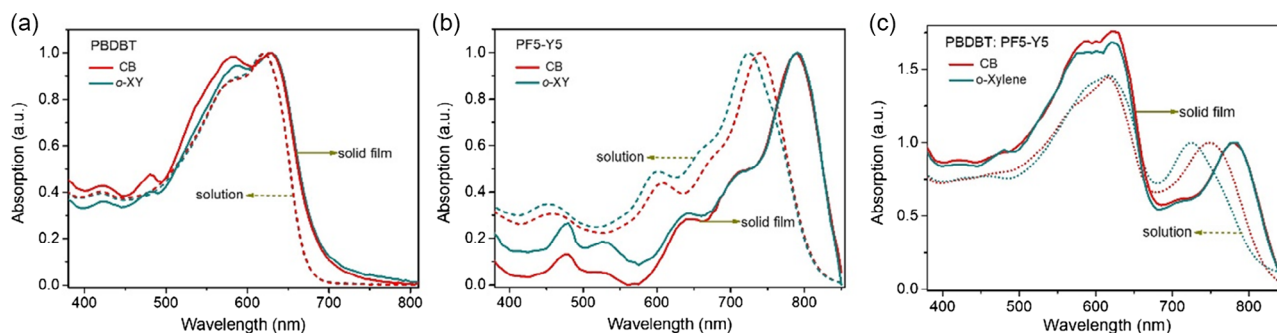


Figure 1. Absorption spectra of a) PBDBT, b) PF5–Y5, and c) PBDBT:PF5–Y5 in chlorobenzene (CB), and *ortho*-xylene (*o*-XY) solutions (dash line), and in solid state (solid line).

monitored using in situ PL spectroscopy. During the drying process, the solutes become compact along with the evaporation of the solvent, leading to the quenching of PL. The PL spectral evolution for neat PBDBT and PF5–Y5 is illustrated in Figure S2, Supporting Information, where *o*-XY with a bit higher boiling point (144 °C) prolongs the drying time compared to CB (132 °C). The emissions of neat PBDBT cast from CB and *o*-XY have similar behaviors with a PL peak around 680 nm and shoulder at 740 nm, and the PL intensity exhibits a smooth decrease. Also, there is no clear spectral shift, which indicates the chain aggregation of PBDBT has already formed in CB and *o*-XY solutions. As for the neat PF5–Y5, the redshifted PL peak at 830 nm is an indicator for the polymer aggregation during film formation. Additionally, the PL intensity evolution shows obvious differences between these two cases, where the PL intensity of CB-cast PF5Y5 decreases continuously, while the *o*-XY one shows almost constant PL intensity at first stage, indicating weak interaction between polymer chains.

Afterward, a significant drop of PL intensity indicates a rapid aggregation at the final stage in *o*-XY.

Regarding the phase behavior for PBDBT:PF5–Y5 BHJs during film formation, **Figure 2a,b** shows in situ PL spectra of PBDBT:PF5–Y5 blends cast from CB and *o*-XY. The initial spectra are dominated by the PF5–Y5 emission with PL maximum at around 850 nm, accompanied by a weaker PL peak at 680 nm originating from PBDBT. The integrated PL intensity of the PBDBT (red dots) and PF5–Y5 (black dots) contributions to the blend spectra are plotted as a function of drying time (Figure 2c,d). The corresponding position of the PL maximum of PF5–Y5 as a function of drying time is shown in Figure 2e,f.

In detail, the PL intensity of PBDBT decreases gradually with drying time in both CB and *o*-XY cast films, while different behaviors of PF5–Y5 signal can be observed. In the case of the CB–BHJ film as shown in Figure 2c, at the first stage, the PL intensity of PF5–Y5 shows faster decrease than *o*-XY one

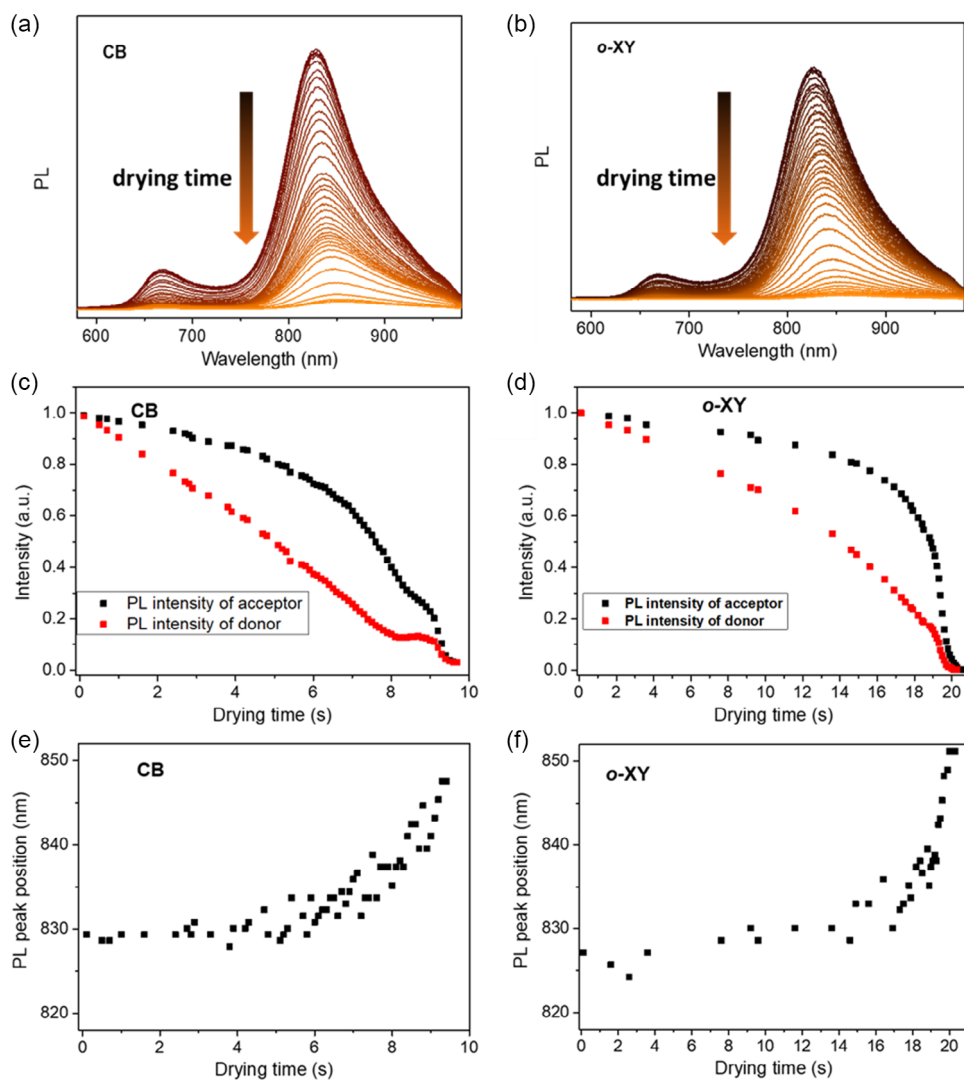


Figure 2. In situ photoluminescence (PL) spectra of PBDBT:PF5–Y5 blend cast from a) CB and b) *o*-XY during film formation process; c,d) the PL intensity of PBDBT (red) and PF5–Y5 (black) were plotted as function of drying time; e,f) the PL peaks of PF5–Y5 during drying are plotted.

(Figure 2d), which indicates stronger interaction between PBDBT and PF5–Y5. Then PF5–Y5 tends to aggregate, leading to the PL drop and peak position shift as shown in Figure 2e. Regarding the *o*-XY–BHJ film, the reduced PL quenching rate can be assigned to the stronger phase separation. As having discussed in absorption characteristics, PF5–Y5 in CB would tend to be unfolded, while PF5–Y5 in *o*-XY solution with coiled chains tends to be self-aggregated. At the final stage, like the neat PF5–Y5 in *o*-XY, the rapid PL quenching (black dots) in Figure 2d is due to the PF5–Y5 aggregation, meanwhile, the peak shift was also observed. It therefore indicates the smaller miscibility between PBDBT and PF5–Y5 for the *o*-XY cast blend film, which leads to larger phase separation.

2.3. TA Spectroscopy

The PL quenching of BHJ films compared to pristine layers is considered as an indicator for charge transfer between donor and acceptor. As shown in Figure S3, Supporting Information, the almost completely PL-quenched CB–BHJ films indicate more efficient charge transfer than *o*-XY–BHJ. Additionally, TA spectroscopy provides information on excitonic and hole-transfer dynamics. CB-cast neat PBDBT and PF5–Y5 exhibit longer exciton lifetime and diffusion length (Figure S4 and Table S1, Supporting Information). Regarding hole-transfer process, an excitation of 800 nm pump laser can selectively excite acceptor PF5–Y5. In Figure 3, the rising signal at 630 nm is induced from PBDBT, which reflects the hole transfer from PF5–Y5 to PBDBT. The hole-transfer dynamics consists of ultrafast charge-transfer process and exciton diffusion process, that can be fitted by a biexponential function

$$I = A_1 \exp\left(-\frac{t}{\tau_1}\right) + A_2 \exp\left(-\frac{t}{\tau_2}\right) \quad (1)$$

Charge transfer at donor/acceptor interface is ultrafast, usually within hundreds of fs (τ_1). Regarding the excitons generated away from the interface usually exhibit relatively slower diffusion process, the exciton diffusion lifetime τ_2 depends on the domain size, where excitons spend long time to diffuse to interface in large domain. As the fitting results shown in Table S2, Supporting Information, these two blend films show comparable ultrafast charge transfer, however, the CB–BHJ film exhibits

shorter exciton diffusion time of ≈ 8.59 ps than the *o*-XY one (≈ 15.3 ps), indicating more efficient hole-transfer and smaller domain size in CB–BHJ films. Considering the exciton diffusion coefficients of the acceptors, the sizes of acceptor phase in the *o*-XY and CB–BHJ films are determined as ≈ 48.1 and ≈ 39.3 nm, respectively. In this case, larger photocurrent will be expected in CB cast solar cells.

2.4. Morphology Characteristics

In addition to the spectroscopy, the ex situ morphology characteristics were also employed. The surface energy of the film components was employed to roughly estimate the miscibility between donor and acceptor in blends. The surface energy was obtained from contact angle measurements using two different test liquids (Figure S5 and Table S3, Supporting Information), where the corresponding values for PBDBT films cast from CB and *o*-XY are 14.8 and 15.5 mN m⁻¹, respectively, while the value for CB-processed PF5–Y5 is 14.1 mN m⁻¹, and *o*-XY-processed PF5–Y5 is 23.6 mN m⁻¹. According to the relation between the Flory–Huggins interaction parameter (χ) and the surface energy^[30,31]

$$\chi \propto (\sqrt{\gamma_i} - \sqrt{\gamma_j})^2 \quad (2)$$

where the $\gamma_{i,j}$ represents the surface energy for the two components, the interaction parameter between the donor and acceptor can be determined. Herein, the big difference in surface energy for *o*-XY cast PBDBT and PF5–Y5 films indicates relatively poor miscibility. Instead, the similar surface energy for donor and acceptor in CB cast films means better miscibility. In addition, from AFM height and phase images of blend films (Figure 4), it is found that (Figure 4a) the surface of the CB-cast blend film ($R_q = 1.00$ nm) shows fiber-like structures, however, coarser surface morphology ($R_q = 2.14$ nm) and large-scale phase separation can be observed in *o*-XY-cast blend films (Figure 4c,d).

Additionally, GIWAXS data as shown in Figure 4e–h and S6, Supporting Information, gives information about crystallinity and ordered structure. These two blend samples show a lamellar peak around 0.30 Å⁻¹ in-plane, with the higher and narrower peak in the CB-cast blend indicating a larger crystal coherence length (CCL) of 57.7 Å, while *o*-XY BHJ has a smaller CCL of 30.6 Å. In the out-of-plane, CB–BHJ still has a bit larger CCL

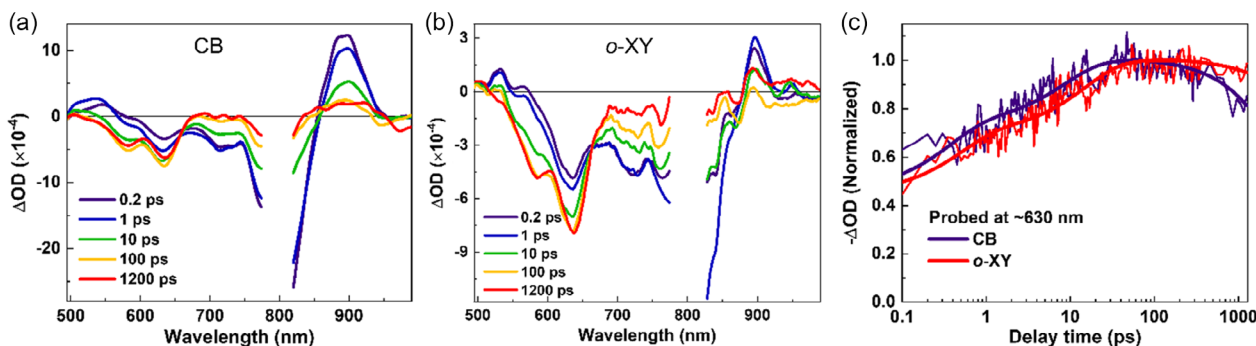


Figure 3. The transient absorption (TA) spectra of PBDBT:PF5–Y5 blend films cast from a) CB and b) *o*-XY; the excited wavelength is 800 nm with an excitation fluency of 2.01×10^{13} photon·pulse⁻¹ cm⁻². c) The extracted dynamics of ≈ 630 nm for PBDBT:PF5–Y5 blend films.

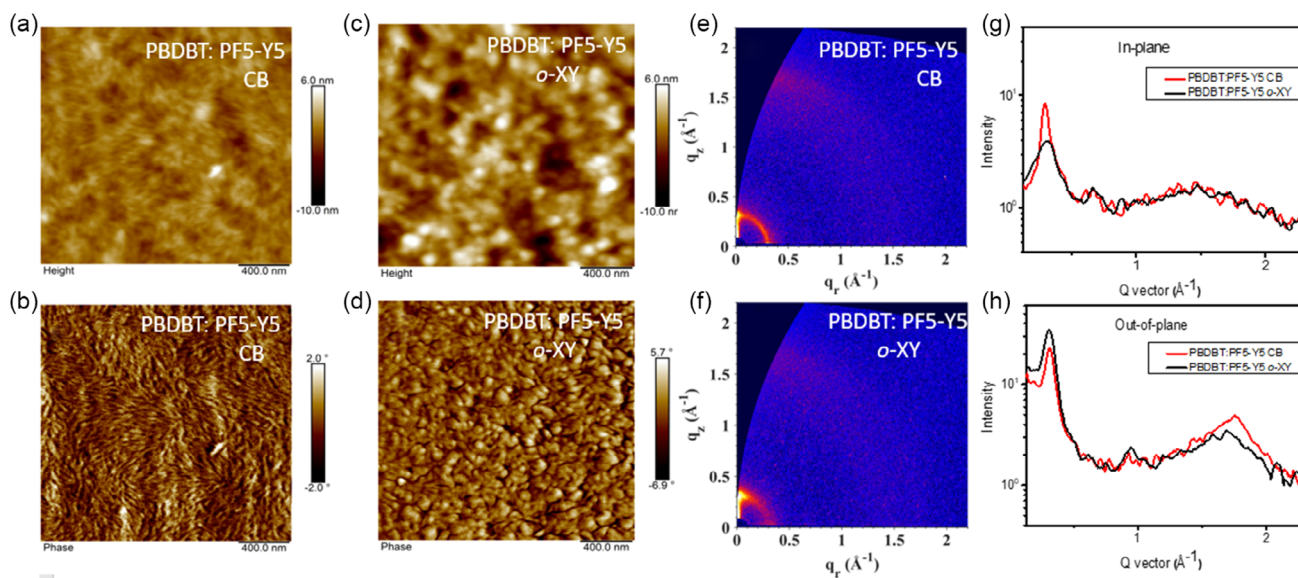


Figure 4. Atomic-force microscopy (AFM) surface morphology and phase images of PBDBT:PF5-Y5 blend films cast from a,b) CB and c,d) *o*-XY. e,f) Grazing-incidence wide-angle X-Ray scattering (GIWAXS) data of g) in-plane and h) out-of-plane of PBDBT:PF5-Y5 blend films cast from CB and *o*-XY.

(58.9 Å) than *o*-XY one (53.8 Å). Regarding the π - π stacking in out-of-plane, the peak of 1.70 \AA^{-1} and CCL of 10.8 \AA for *o*-XY-BHJ, the peak of 1.75 \AA^{-1} and CCL of 13.3 \AA for CB-BHJ, the higher intensity and peak shift indicate a smaller π - π stacking distance and relatively more ordered structure in CB-blend film.

2.5. Photovoltaic Performance and Energy Loss of All-PSCs

The results provided previously have demonstrated different film formation processes and morphology for blend films caused by processing solvents. Such difference could influence charge-carrier dynamics, thereby affecting output performance of devices. To study how these different morphology evolution influence device performance, the all-PSCs were fabricated with structure of ITO/PEDOT:PSS/PBDBT:PF5-Y5/2,9-bis[3-(dimethylamino)propyl]anthra[2,1,9-def:6,5,10-d'e'f']diisoquinoline-1,3,8,10(2H,9H)-tetrone (PDINO)/Al, where the active layers were prepared by blade-coating methods in air. Current density-voltage (J - V) characteristics and external quantum efficiency (EQE) spectra for CB- and *o*-XY-processing solar cells were measured in air and shown in Figure S7, Supporting Information. This all-PSC with CB as solvent exhibits higher efficiency of 8.66% than *o*-XY device (Table 1). The higher short-circuit current density (J_{SC}) of 15.7 mA cm^{-2} in CB device is attributed to the better mixed donor/acceptor and smaller-scale phase separation, while the less donor/acceptor miscibility and large-scale phase separation could suppress charge generation, lowering photocurrent in *o*-XY device. The PL and TA characteristics also consist with the photocurrent of solar cells.

The device FFs (0.60 vs 0.50) also indicate different charge-transport profiles. To compare the charge-transport properties between these two BHJs, hole and electron mobilities were extracted from dark J - V curve of signal-layer solar cells (Figure S8, Supporting Information). In Table 1, both electron and hole mobilities of *o*-XY-processed device are lower than that

Table 1. Photovoltaic parameters of CB- or *o*-XY-processed PBDBT:PF5-Y5 BHJ-based solar cells, and the hole and electron mobilities.

Solvent	J_{sc} [mA cm^{-2}]	FF	V_{OC} [V]	PCE [%]	μ_h [$\text{cm}^2 \text{ V}^{-1} \text{ s}^{-1}$]	μ_e [$\text{cm}^2 \text{ V}^{-1} \text{ s}^{-1}$]	μ_h/μ_e
CB	15.7	0.60	0.92	8.66 (8.39) ^{a)}	1.36×10^{-4}	8.38×10^{-5}	1.62
<i>o</i> -XY	12.7	0.50	0.87	5.52 (5.38) ^{a)}	5.80×10^{-5}	5.25×10^{-6}	11.0

^{a)}The data in brackets are average values with standard deviation from ten devices.

of CB device. Especially the electron mobility for *o*-XY-processed devices is one order of magnitude smaller than that of CB-processed ones, the slope change in dark J - V curve of electron-only device (Figure S8b, Supporting Information) indicates electron trapping in *o*-XY device. The poor charge-transport accounts for the smaller FF in *o*-XY-processed devices.

Regarding the difference in V_{OC} for these two solar cells, the energetic disorder was analyzed, as the presence of disorder would bring severe non-radiative recombination and then lead to more energy loss for solar cells. The energetic disorder was obtained from Gaussian disorder model by temperature-dependent space charge-limited current (SCLC) measurement. As the results shown in Figure 5 and S8, Supporting Information, CB-cast hole-only device shows comparable disorder (66 meV) to *o*-XY-processed one (67 meV), while in terms of electron-only devices, a larger disorder of 81 meV was observed in *o*-XY device and CB device has a much smaller one of 71 meV. This is consistent with the GIWAXS data, where CB-cast blend film exhibits more ordered structure and longer CCL than the *o*-XY-processed blend. The larger disorder in *o*-XY device means broad DOS, which can also be confirmed by broader electroluminescence (EL) spectra (Figure S9, Supporting Information).

Herein, to quantify and understand the difference in V_{OC} , the detailed energy loss was investigated. The total energy loss can be given by

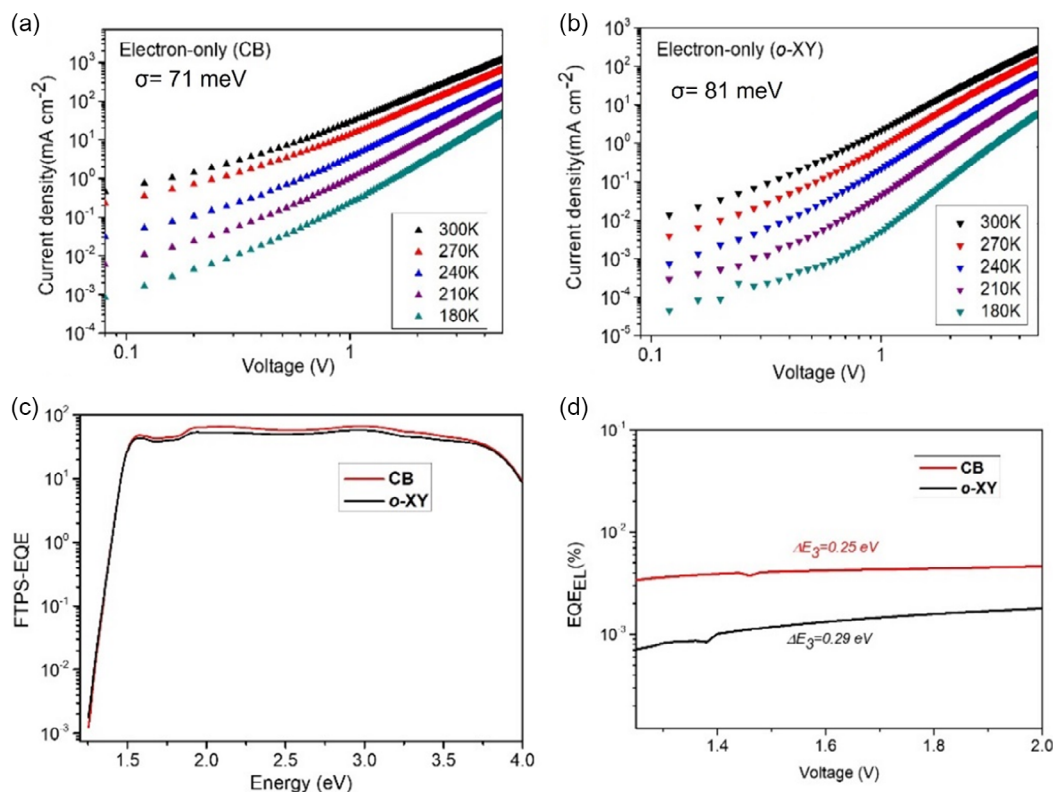


Figure 5. Dark current density–voltage (J – V) curves for electron-only devices based on a) CB and b) *o*-XY cast PBDBT:PF5-Y5 BHJs under different temperature. c) Fourier-transform photocurrent spectroscopy external quantum efficiency (FTPS-EQE) and d) EQE_{EL} curves of CB- and *o*-XY-processed PBDBT:PF5-Y5 bulk-heterojunctions (BHJ)-based all-PSCs.

$$\begin{aligned} \Delta E_{\text{loss}} &= E_g - qV_{\text{oc}} \\ &= (E_g - qV_{\text{oc}}^{\text{SQ}}) + (qV_{\text{oc}}^{\text{SQ}} - qV_{\text{oc}}^{\text{rad}}) + (qV_{\text{oc}}^{\text{rad}} - qV_{\text{oc}}) \\ &= (E_g - qV_{\text{oc}}^{\text{SQ}}) + q\Delta V_{\text{oc}}^{\text{rad, below gap}} + q\Delta V_{\text{oc}}^{\text{non-rad}} \\ &= \Delta E_1 + \Delta E_2 + \Delta E_3 \end{aligned} \quad (3)$$

where the photovoltaic bandgap E_g was obtained from EQE (Figure 5c), ΔE_1 and ΔE_2 represent radiative loss above and below bandgap, respectively, ΔE_3 is the non-radiative loss, which can be calculated from electroluminescence EQE (EQE_{EL}) of devices (Figure 5d)

$$\Delta E_3 = q\Delta V_{\text{oc}}^{\text{non-rad}} = -kT \ln(EQE_{EL}) \quad (4)$$

As the detailed voltage losses shown in **Table 2**, the different ΔE_{loss} between CB (0.54 eV) and *o*-XY (0.59 eV) processed-solar cells is dominated by non-radiative recombination ΔE_3 , where CB device has ΔE_3 of 0.25 eV and *o*-XY-device has ΔE_3 of 0.29 eV. The smaller non-radiative voltage loss in CB device contributes to the relatively larger V_{OC} (0.92 V). In terms of *o*-XY-device with larger ΔE_3 , we have known this system suffers from large energetic disorder, and the trapped charges in the tail states will limit charge transport and cause more non-radiative recombination. Additionally, regarding the system with broad DOS, the charges would first occupy the tail states, that limits the splitting of quasi-Fermi levels for electrons and holes. As a result,

Table 2. Detailed energy loss of CB- and *o*-XY-processed PBDBT:PF5-Y5 BHJ-based all-PSCs.

Solvent	E_g [eV]	$V_{\text{oc}}^{\text{SQ}}$ [V]	$V_{\text{oc}}^{\text{rad}}$ [V]	ΔE_1 [V]	ΔE_2 [V]	ΔE_3 [V]	ΔE_{loss} [eV]
CB	1.47	1.21	1.18	0.26	0.03	0.25	0.54
<i>o</i> -XY	1.48	1.21	1.18	0.27	0.03	0.29	0.59

the V_{OC} will be reduced. Therefore, less disorder is crucial to further improve the device performance with small voltage loss.

3. Conclusion

A comparative study based on blade-coated PBDBT:PF5-Y5 all-PSCs was performed using CB and *o*-XY as processing solvents. The film-drying process was monitored by in situ optical spectra, which demonstrates better donor/acceptor miscibility in CB-cast film, thereby facilitating charge generation and higher photocurrent. Additionally, the relatively ordered structure is beneficial for charge transport and reduced non-radiative loss, which results in higher FF and V_{OC} in CB-processed devices than the *o*-XY ones. These results indicate that polymer chain conformations and aggregation in solution will persist in the solid state. It is crucial to achieve ordered structure and aggregation in the initial stage in solution for improving photovoltaic performance of all-PSCs.

4. Experimental Section

Materials: PBDBT and PDINO were purchased from Solarmer, Inc. (Beijing). Poly(3,4-ethylenedioxythiophene):polystyrene sulfonate (PEDOT:PSS, Al 4083) was purchased from Heraeus. ZnO (N-10, 2.5 wt% in isopropanol) was purchased from Avantama. PF5–Y5 was synthesized according to the previous work. All materials were used as received without additional purification.

Device Fabrication: All-PSCs were prepared with conventional structure of ITO/PEDOT:PSS/PBDBT:PF5–Y5/PDINO/Al. All the functional layers except active layer were prepared according to our previous article.^[32] PBDBT:PF5–Y5 with weight ratio of 1:0.75 were dissolved in CB or *o*-XY with a total concentration of 16 mg mL⁻¹. The blend solutions were stirred at 80 °C for 6 h before blade-coating. The active layers were blade-coated on ITO/PEDOT:PSS in air, during blade-coating process, the ITO substrates were placed on hot plate with temperature of 60 °C. The active layers (120 nm) were subsequently thermal annealed at 100 °C for 10 min in glove box. After that PDINO was spin-coated on the active layers. Finally, 100 nm of Al was thermally evaporated through shadow mask in a vacuum 1 × 10⁻⁶ mbar. The effective device area of devices is 0.047 cm².

Characterizations: Absorption spectra were measured by a Perkin Elmer Lambda 900 UV–Vis–NIR spectrometer. In situ optical spectroscopy setup was reported in previous work. A 532 nm laser was used as excitation source, and the PL spectra and laser signals were recorded by QE-Pro spectrometer. The *J*–*V* curves were characterized by a Keithley 2400 source meter with AM 1.5 G solar simulator at an intensity of 100 mW cm⁻². AFM images were measured with a Dimension 3100. GIWAXS was measured with a Xeuss 2.0 WAXS laboratory beamline at The Chinese University of Hong Kong. Contact angles were measured with CAM 200 optical contact angle meter.

Femtosecond TA measurements were carried out by home-built TA system. The light source of the TA system was a femtosecond laser out from a regenerative amplifier (Legend Elite F 1 K HE + II, Coherent), operating at 800 nm with a repetition rate of 1 kHz. The fundamental light was divided into two parts. One part of the light was frequency doubled (400 nm) or used directly as the pump light. The other part was used to excite a sapphire plate for the generation of supercontinuum white light, which was further used as the probing light for differential absorption measurement. The probing light was guided into a monochromator (Omni-λ200i, Zolix) and detected by a charge-coupled device detector (Pascher Instrument). The pump “on” and “off” for a pair of sequential actinic pulse was regulated by a mechanical chopper (500 Hz, MC2000B-EC, Thorlabs) in the pump beam. With the help of a mechanical delay line, the probe was time delayed relative to the pump. TA spectroscopy was used to study the properties of pristine donor, acceptor, and blends. We fitted the exciton lifetime τ ($\tau = 1/k$), annihilation rate constant γ according to the decay signals under various excitation fluence

$$\frac{dn(t)}{dt} = -kn(t) - \frac{1}{2}\gamma n(t)^2 \quad (5)$$

$$n(t) = \frac{n(0)\exp(-kt)}{1 + \frac{\gamma}{2k}n(0)[1 - \exp(-kt)]} \quad (6)$$

In addition, the exciton diffusion coefficient *D*, exciton diffusion length *L_d*, and phase size *L_s* were obtained according to the equations

$$D = \frac{\gamma}{8\pi R} \quad (7)$$

$$L_d = \sqrt{D\tau} \quad (8)$$

$$L_s = 2\sqrt{6D\tau_2} \quad (9)$$

where *R* is the annihilation radius of singlet excitons, τ_2 is exciton–diffusion-mediated lifetime.

Energy loss analysis: Electroluminescence spectra were recorded with an Andor spectrometer. The FTPS-EQE was measured by a Vertex 70 (Bruker Optics). The EQE_{EL} was measured by an in-house-built system

with a silicon photodiode. Herein, the photovoltaic bandgap energy *E_g* was obtained from EQE of solar cells, *E_g* as the mean peak energy at the absorption edge of the distribution *P*(*E*) is given by

$$E_g = \frac{\int_a^b EP(E)dE}{\int_a^b P(E)dE} \quad (10)$$

where the integration intervals *a* and *b* are chosen when the energy is equal to half of maximum *P*(*E*), $P(a) = P(b) = P(E)_{\max}/2$.

The *V_{OC}* based on Shockley–Queisser theory *V_{OC}^{SQ}* can be calculated as

$$V_{oc}^{SQ} = \frac{kT}{q} \ln \left(\frac{J_{sc}^{SQ}}{J_0^{SQ}} + 1 \right) = \frac{kT}{q} \ln \left(\frac{q \int EQE_{PV}^{SQ}(E) \Phi_{AM1.5g}(E) dE}{q \int EQE_{PV}^{SQ}(E) \Phi_{BB}(E) dE} + 1 \right) \quad (11)$$

When all recombination is radiative, *V_{OC}^{rad}* is given by

$$V_{oc}^{rad} = \frac{kT}{q} \ln \left(\frac{J_{sc}^{rad}}{J_0^{rad}} + 1 \right) = \frac{kT}{q} \ln \left(\frac{q \int EQE_{PV}(E) \Phi_{AM1.5g}(E) dE}{q \int EQE_{PV}(E) \Phi_{BB}(E) dE} + 1 \right) \quad (12)$$

where *k* is the Boltzmann constant, *T* is the ambient temperature, *q* is the elementary charge.

$$\Delta E_1 = E_g - qV_{oc}^{SQ} \quad (13)$$

$$\Delta E_2 = qV_{oc}^{SQ} - qV_{oc}^{rad} \quad (14)$$

$$\Delta E_3 = -kT \ln(EQE_{EL}) \quad (15)$$

Supporting Information

Supporting Information is available from the Wiley Online Library or from the author.

Acknowledgements

N.Y., F.Z., J.v.S., E.M., and E.W. acknowledge funding from the Knut and Alice Wallenberg foundation under contract 2016.0059. N.Y. and F.Z. acknowledge funding from the Swedish Government Research Area in Materials Science on Functional Materials at Linköping University (Faculty Grant SFO-Mat-LiU No. 200900971) and China Scholarship Council (CSC) (No. 201708370115). E.W. further acknowledges the Knut and Alice Wallenberg foundation (2017.0186), the Swedish Research Council and the Swedish Energy Agency for financial support. W.Z. acknowledges funding from the National Natural Science Foundation of China (Grant no. 21903017).

Conflict of Interest

The authors declare no conflict of interest.

Data Availability Statement

The data that support the findings of this study are available from the corresponding author upon reasonable request.

Keywords

blade-coated solar cells, all-polymer solar cells, energetic disorder, energy losses, in situ photoluminescence, morphology evolution

Received: December 28, 2022

Revised: January 16, 2023

Published online:

- [1] T. Kim, J. H. Kim, T. E. Kang, C. Lee, H. Kang, M. Shin, C. Wang, B. Ma, U. Jeong, T. S. Kim, B. J. Kim, *Nat. Commun.* **2015**, *6*, 8547.
- [2] H. Kang, W. Lee, J. Oh, T. Kim, C. Lee, B. J. Kim, *Acc. Chem. Res.* **2016**, *49*, 2424.
- [3] H. Sun, Y. Tang, C. W. Koh, S. Ling, R. Wang, K. Yang, J. Yu, Y. Shi, Y. Wang, H. Y. Woo, X. Guo, *Adv. Mater.* **2019**, *31*, 1807220.
- [4] C. Lee, S. Lee, G. U. Kim, W. Lee, B. J. Kim, *Chem. Rev.* **2019**, *119*, 8028.
- [5] Q. Fan, W. Su, S. Chen, W. Kim, X. Chen, B. Lee, T. Liu, U. A. Méndez-Romero, R. Ma, T. Yang, W. Zhuang, Y. Li, Y. Li, T. S. Kim, L. Hou, C. Yang, H. Yan, D. Yu, E. Wang, *Joule* **2020**, *4*, 658.
- [6] C. R. McNeill, *Energy Environ. Sci.* **2012**, *5*, 5653.
- [7] Y. Lin, J. Wang, Z. G. Zhang, H. Bai, Y. Li, D. Zhu, X. Zhan, *Adv. Mater.* **2015**, *27*, 1170.
- [8] J. Yuan, Y. Zhang, L. Zhou, G. Zhang, H. L. Yip, T. K. Lau, X. Lu, C. Zhu, H. Peng, P. A. Johnson, M. Leclerc, Y. Cao, J. Ulanski, Y. Li, Y. Zou, *Joule* **2019**, *3*, 1140.
- [9] Y. Cui, Y. Xu, H. Yao, P. Bi, L. Hong, J. Zhang, Y. Zu, T. Zhang, J. Qin, J. Ren, Z. Chen, C. He, X. Hao, Z. Wei, J. Hou, *Adv. Mater.* **2021**, *33*, 2102420.
- [10] L. Zhu, M. Zhang, J. Xu, C. Li, J. Yan, G. Zhou, W. Zhong, T. Hao, J. Song, X. Xue, Z. Zhou, R. Zeng, H. Zhu, C. Chen, R. C. I. Mackenzie, Y. Zou, J. Nelson, Y. Zhang, Y. Sun, F. Liu, *Nat. Mater.* **2022**, *21*, 656.
- [11] Z. G. Zhang, Y. Li, *Angew. Chem. Int. Ed.* **2021**, *60*, 4422.
- [12] Q. Fan, Q. An, Y. Lin, Y. Xia, Q. Li, M. Zhang, W. Su, W. Peng, C. Zhang, F. Liu, L. Hou, W. Zhu, D. Yu, M. Xiao, E. Moons, F. Zhang, T. D. Anthopoulos, O. Inganäs, E. Wang, *Energy Environ. Sci.* **2020**, *13*, 5017.
- [13] W. Wang, Q. Wu, R. Sun, J. Guo, Y. Wu, M. Shi, W. Yang, H. Li, J. Min, *Joule* **2020**, *4*, 1070.
- [14] J. Du, K. Hu, J. Zhang, L. Meng, J. Yue, I. Angunawela, H. Yan, S. Qin, X. Kong, Z. Zhang, B. Guan, H. Ade, Y. Li, *Nat. Commun.* **2021**, *12*, 5264.
- [15] Y. Zhang, B. Wu, Y. He, W. Deng, J. Li, J. Li, N. Qiao, Y. Xing, X. Yuan, N. Li, C. J. Brabec, H. Wu, G. Lu, C. Duan, F. Huang, Y. Cao, *Nano Energy* **2022**, *93*, 106858.
- [16] F. Zhang, K. G. Jespersen, C. Björström, M. Svensson, M. R. Andersson, V. Sundström, K. Magnusson, E. Moons, A. Yartsev, O. Inganäs, *Adv. Funct. Mater.* **2006**, *16*, 667.
- [17] H. Cha, Y. Li, S. Kim, Y. Kim, S. Kwon, *Macromol. Res.* **2020**, *28*, 820.
- [18] F. Gao, S. Himmelberger, M. Andersson, D. Hanifi, Y. Xia, S. Zhang, J. Wang, J. Hou, A. Salleo, O. Inganäs, *Adv. Mater.* **2015**, *27*, 3868.
- [19] Y. Liu, A. Yangui, R. Zhang, A. Kiligaridis, E. Moons, F. Gao, O. Inganäs, I. G. Scheblykin, F. Zhang, *Small Methods* **2021**, *5*, 2100585.
- [20] J. J. Van Franeker, M. Turbiez, W. Li, M. M. Wienk, R. A. J. Janssen, *Nat. Commun.* **2015**, *6*, 6229.
- [21] S. Engmann, F. A. Bokel, H. W. Ro, D. M. DeLongchamp, L. J. Richter, *Adv. Energy Mater.* **2016**, *6*, 1502011.
- [22] J. Min, N. S. Güldal, J. Guo, C. Fang, X. Jiao, H. Hu, T. Heumüller, H. Ade, C. J. Brabec, *J. Mater. Chem. A* **2017**, *5*, 18101.
- [23] J. O. Oelerich, F. Jansson, A. V. Nenashov, F. Gebhard, S. D. Baranovskii, *J. Phys. Condens. Matter* **2014**, *26*, 255801.
- [24] A. Karki, G. J. A. H. Wetzelaer, G. N. M. Reddy, V. Nádaždy, M. Seifrid, F. Schauer, G. C. Bazan, B. F. Chmelka, P. W. M. Blom, T. Q. Nguyen, *Adv. Funct. Mater.* **2019**, *29*, 1901109.
- [25] J. C. Blakesley, D. Neher, *Phys. Rev. B* **2011**, *84*, 075210.
- [26] Q. Bian, B. A. Abdulahi, Z. Genene, E. Wang, W. Mammo, O. Inganäs, *J. Phys. Chem. Lett.* **2020**, *11*, 3796.
- [27] F. Zhao, D. He, C. Zou, Y. Li, K. Wang, J. Zhang, S. Yang, Y. Tu, C. Wang, Y. Lin, *Adv. Mater.* **2022**, 2210463.
- [28] X. Chen, D. Qian, Y. Wang, T. Kirchartz, W. Tress, H. Yao, J. Yuan, M. Hülsbeck, M. Zhang, Y. Zou, Y. Sun, Y. Li, J. Hou, O. Inganäs, V. Coropceanu, J. Bredas, F. Gao, *Nat. Energy* **2021**, *6*, 799.
- [29] T. Q. Nguyen, V. Doan, B. J. Schwartz, *J. Chem. Phys.* **1999**, *110*, 4068.
- [30] P. Becher, *J. Colloid Interface Sci.* **1977**, *59*, 429.
- [31] S. Nilsson, A. Bernasik, A. Budkowski, E. Moons, *Macromolecules* **2007**, *40*, 8291.
- [32] N. Yao, J. Wang, Z. Chen, Q. Bian, Y. Xia, R. Zhang, J. Zhang, L. Qin, H. Zhu, Y. Zhang, F. Zhang, *J. Phys. Chem. Lett.* **2021**, *12*, 5039.